



# Optimization of 4D flow MRI velocity field in the aorta with divergence-free smoothing

Qi Gao<sup>1</sup> · Xingli Liu<sup>2</sup> · Hongping Wang<sup>3</sup> · Peng Wu<sup>4</sup> · Mansu Jin<sup>2</sup> · RunJie Wei<sup>2</sup> · Wei Wang<sup>5</sup> · Zhaozhao Niu<sup>6</sup> · Shihua Zhao<sup>7</sup> · Fei Li<sup>5,8</sup>

Received: 11 August 2020 / Accepted: 14 July 2021 / Published online: 15 September 2021  
© International Federation for Medical and Biological Engineering 2021

## Abstract

Divergence-free smoothing with wall treatment (DFS<sub>w</sub>) method is proposed for processing with four-dimensional (4D) flow magnetic resonance imaging (MRI) data of blood flows to enhance the quality of flow field with physical constraints. The new method satisfies the no-slip wall boundary condition and applies wall function of velocity profile for better estimating the velocity gradient in the near-wall region, and consequently improved wall shear stress (WSS) calculation against the issue of coarse resolution of 4D flow MRI. In the first testing case, blood flow field obtained from 4D flow MRI is well smoothed by DFS<sub>w</sub> method. A great consistency is observed between the post-processed 4D flow MRI data and the computational fluid dynamics (CFD) data in the interested velocity field. WSS has an apparent improvement due to the proposed near-wall treatment with special wall function comparing to the result from original 4D flow MRI data or the DFS-processed data with no wall function. The other five cases also show the same performance that smoothed velocity field and improved WSS estimation are achieved on 4D flow MRI data optimized by DFS<sub>w</sub>. The improvements will benefit the study of hemodynamics regarding the determination of location or the potential possibility of lesions.

**Keywords** 4D flow MRI · Computational fluid dynamics · Wall shear stress · Divergence-free smoothing

## 1 Introduction

In recent years, four-dimensional (4D) flow magnetic resonance imaging (MRI) has become popular in vivo research and clinical medicine as a new potential diagnostic tool [1], referring to time-resolved three-dimensional (3D) phase-contrast (PC) MRI with 3D flow encoding [2]. In addition to providing morphological information, it also permits the

acquisition of functional information and further obtains the hemodynamic index [3, 4] within a vascular region of interest.

Increasingly, 4D flow MRI is applied to investigate the mechanism of aortic blood flow and to explore the pathogenesis of aortic diseases [5, 6], such as aortic aneurysm and aortic dissection [7]. The formation of these diseases may be related to the blood flow pattern inside the aorta, and the occurrence of pathology will further change the pattern of

✉ Qi Gao  
qigao@zju.edu.cn

✉ Shihua Zhao  
cjrzaoshihua2009@163.com

✉ Fei Li  
lifei@fuwaihospital.org

<sup>1</sup> School of Aeronautics and Astronautics, Zhejiang University, Yuquan Campus, 38 Zheda Road, Xihu District, Hangzhou 310027, China

<sup>2</sup> Hangzhou Shengshi Technology Co., Ltd., Hangzhou, China

<sup>3</sup> The State Key Laboratory of Nonlinear Mechanics, Institute of Mechanics, Chinese Academy of Sciences, Beijing, China

<sup>4</sup> Artificial Organ Technology Lab, Bio-manufacturing Research Centre, School of Mechanical and Electric Engineering, Soochow University, Suzhou, China

<sup>5</sup> Department of Structural Heart Disease, Chinese Academy of Medical Sciences & Fuwai Hospital; State Key Laboratory of Cardiovascular Disease, Peking Union Medical College, 167 Beilishi Road, Xicheng District, 100037 Beijing, China

<sup>6</sup> Cardiac Surgery, Qingdao Municipal Hospital, Qingdao, China

<sup>7</sup> Department of Magnetic Resonance Imaging, Chinese Academy of Medical Sciences & Fuwai Hospital, Peking Union Medical College, 167 Beilishi Road, Xicheng District, 100037 Beijing, China

<sup>8</sup> Department of Cardiac Surgery, Peking University First Hospital, Beijing, China

blood flow, thereby aggravating the lesion or triggering new ones [8, 9]. In the past few years, wall shear stress (WSS) calculated from the velocity field of 4D flow MRI has become a new potential diagnostic indicator for diseases [10–13]. However, the velocity field measured from 4D flow MRI contains experimental errors or noises, which will significantly affect the visualization of flow field and computing accuracy of hemodynamic parameters.

4D flow MRI data can be well processed by mathematical methods [14, 15]. However, the post-processed results normally do not satisfy the physical constraints (or governing laws), such as Navier–Stokes equations (NS equations). The simplest physical constraint for hemodynamics is the mass conservation, namely divergence-free condition, which can be used to improve the 4D flow MRI data. For instance, Song et al. [16] projected the MRI velocity field into a divergence-free space by finite difference method to achieve the goal of improving signal-to-noise (S/N). Busch et al. [17] and Ong et al. [18] implemented fast and efficient divergence-free correction of MRI velocity field by divergence-free radial basis functions and diverging-free wavelets, respectively. The divergence-free smoothing (DFS) method [19] can minimize the deviation between the revised flow field and the measured flow field, and further smooth flow field simultaneously, which was proposed for optimizing the volumetric particle image velocimetry (PIV) data in experimental fluid mechanics. Many methods have been used for post-processing of flow field, but they did not pay much attention to the property of divergence in flow field. When DFS was proposed in reference [19], the authors well demonstrated the divergence-free performance among various post-processing methods. Based on their investigation, it can be easily expected that DFS would be the best approach for data processing on 4D flow MRI if divergence-free behavior is considered. Due to the similarity of data structures of volumetric PIV data and 4D flow MRI data, velocity field of 4D flow MRI can be well processed by the DFS method as well. However, the original DFS method in the article was applied for external velocity field, and it did not provide a near-wall treatment to satisfy no-slip boundary condition (zero velocity) at the wall in an internal flow. Thus, available divergence-free post-processing techniques typically do not meet boundary conditions.

As a very important hemodynamic indicator, WSS can be estimated using the spatial derivative of near-wall tangential velocity calculated by numerical differentiation [20] and a linear least squares method [10]. The accuracy of WSS will be influenced by many facts, such as low resolution or poor signal-to-noise ratio measurement of velocity gradient. Therefore, relying on the vascular model and velocity distribution, Potters et al. [21] acquired the velocity distribution near the vessel wall using a cubic spline curve of natural adjacent point interpolation, while Rimirasih et al. [22] fitted the near-wall velocity profile to the paraboloid utilizing

velocity within the 80 to 95% radius of the aorta. Both of these methods built relatively accurate velocity profiles to compute the WSS. However, general fitting methods are normally from mathematical tools with less physical meaning associated with fluid viscosity near the wall.

In the current work, a DFS with wall treatment (DFS<sub>wl</sub>) method is introduced for processing 4D flow MRI data of blood flows in aortas to improve the quality of flow field with physical constraints. The method we developed satisfies the no-slip boundary condition for the wall-bounded flow and minimizes the deviation between the revised flow field and the measured flow field. Meanwhile, considering the profiles of blood velocity in the log-linear region, velocity profile was fitted by binomial using Musker wall function [23] for better calculating the WSS. Then, velocity field and WSS coming from 4D flow MRI of the first testing case are discussed in comparison with that computed from CFD to clarify the feasibility of DFS<sub>wl</sub> method. At last, the other five cases are used to validate the applicability and the robustness of DFS<sub>wl</sub> method for processing 4D flow MRI data.

## 2 Methods

### 2.1 Patients and MRI data acquisition

Six patients with ascending aortic aneurysm complicated with aortic regurgitation were selected for this study. MRI was performed on the patient using a 3.0 Tesla MR scanner (Discovery MR750, GE Healthcare, Waukesha, WI, USA), and 4D flow MRI sequences were used to obtain the blood flow data on three mutually perpendicular dimensions simultaneously. The scan parameters have been described in detail in our previous studies [24].

### 2.2 Morphologic reconstruction

4D flow MRI velocity field consists of a total number of 80 magnitude images and 80×3 velocity images, with which the 3D velocity field and aorta are reconstructed. Two neighborhood methods, named neighborhood variance method [25] and neighborhood sign determination method, are respectively used to determine crude outline of the aorta. To be specific, the raw image signal of velocity in the inner region of the aorta is relatively consistent, while the signal in other regions shows extremely high level of noise that cannot be considered velocity. The signal intensity gradient between the neighboring points in those regions is much larger than that in the aortic area, normally more than 10 times. Therefore, the larger noise area in 4D flow MRI data can be suppressed by the neighborhood variance method, and then distinguish the aortic area. However, neighborhood variance method cannot perfectly mark the aortic region. Therefore, we proposed neighborhood

sign determination method at each pixel to calculate the number of same velocity sign in its neighborhood. The neighborhood sign determination method has a higher response to the area where the velocity direction is more consistent. According to this feature, it can distinguish the aortic region from other areas. The combination of neighborhood variance method and neighborhood sign determination method can effectively amplify the region feature of interest and reveal the outline of the aorta. Specifically, the procedures for determining the aortic area are as follows:

Step 1: The variance of each velocity component is computed by neighborhood variance method firstly.

Step 2: The maximum variance is subtracted from the velocity variance data. And then, new velocity variance data is obtained by taking the absolute value of the variance for each velocity component.

Step 3: Subsequently, the amount of the same velocity sign of each velocity component is computed by neighborhood sign determination method.

Step 4: A dot product between the variance and the number of the same local velocity sign is applied to each velocity component.

Step 5: At last, the crude outline of the aorta can be determined by the summation of the dot products of all velocity components.

The formulas of neighborhood variance method (Eq. 1) and neighborhood sign determination method (Eq. 2) are given as follows:

$$I_S(i, j) = \sqrt{\frac{1}{mn} \sum_{(x,y) \in S} (f_S(x, y) - \bar{f}_S)^2} \tag{1}$$

and

$$PN_S(i, j) = |length_S(P) - length_S(N)|^2 \tag{2}$$

where  $S$  is the region of the neighborhood,  $m$  and  $n$  are dimensions of  $S$ ,  $(x, y)$  is the local coordinates of  $S$ ,  $f_S(x, y)$  is the intensity of point  $(x, y)$ ,  $\bar{f}_S$  is the average intensity in  $S$ ,  $I_S(i, j)$  is the variance in  $S$  centered at point  $(i, j)$ ,  $(i, j)$  is the global coordinates of the raw image,  $length_S(P)$  is the number of pixels with positive intensity in  $S$ , and  $length_S(N)$  is the number of pixels with negative intensity in  $S$ .

All residual noise is eliminated using the median filter method [26] to the images processed by two neighborhood methods. Then, automatic threshold segmentation of images is proceeded using Otsu’s method to produce final images which can be used to extract the aorta model [27]. To be specific, a segmentation threshold is obtained from gray-level histograms using the Otsu method for the filtered image. Then, it can be used to mark the target area. More details have been given in reference [27]. A 3D model with the form of points cloud is preliminarily generated by merging all of the

denoised images with the pattern of original slices of 4D flow MRI. Finally, a 3D aortic morphological model is obtained by using the Poisson surface reconstruction that transforms the points cloud into surface [28]. The 4D flow MRI data processing strategy and the model of the first testing case is shown in Fig. 1.

### 2.3 New model of near-wall velocity for WSS calculation

Under the hypothesis that blood vessel is inelastic, the velocity of 4D flow MRI at the vessel wall is zero according to the no-slip boundary condition. However, the original DFS method does not provide a near-wall treatment satisfying boundary conditions [19], and the greatest difficulty in applying DFS to 4D flow MRI is how to deal with no-slip wall condition. This section will detail the process of establishing DFS<sub>w</sub> equations through a blood vessel model.

Figure 2 shows the 2D diagram of the velocity grid and vessel wall (solid black curve). The velocity of 4D flow MRI locates at the inner grid. Take two points A and B in the figure as an example to establish the difference equation in the near-wall region. They are nearest points along normal directions of the wall with spacing to the wall as  $dx(dx > 0)$  and  $dy(dy > 0)$ , respectively. Both of them are smaller than the grid spacing  $h$ , which means the location of the wall has a sub-grid precision. Taylor expansion of velocities at point A is

$$u_0 = u_1 - \left(\frac{\partial u}{\partial x}\right)_0 dx + \frac{1}{2} \left(\frac{\partial^2 u}{\partial x^2}\right)_0 dx^2 + O(dx^3) \tag{3}$$

$$u_2 = u_1 + \left(\frac{\partial u}{\partial x}\right)_0 h + \frac{1}{2} \left(\frac{\partial^2 u}{\partial x^2}\right)_0 h^2 + O(h^3) \tag{4}$$

Let  $\theta = dx/h$ , the derivatives in Eqs. (3) and (4) become

$$\left(\frac{\partial u}{\partial x}\right)_0 = \frac{1}{h} \left(-\frac{1}{\theta^2 + \theta} u_0 + \frac{1-\theta}{\theta} u_1 + \frac{\theta}{1+\theta} u_2\right) \tag{5}$$

$$\left(\frac{\partial^2 u}{\partial x^2}\right)_0 = \frac{2}{h^2} \left(\frac{1}{\theta^2 + \theta} u_0 - \frac{1}{\theta} u_1 + \frac{1}{1+\theta} u_2\right) \tag{6}$$

Similar expansions of velocities at point B could be achieved. For the grid points in the near-wall region, the difference equations need to be re-established according to Eqs. (5) and (6), while the central difference scheme is applied at the inner points far from the wall boundary.

In the DFS<sub>w</sub> method, the divergence of the smoothed velocity field needs to be zero. At the same time, the difference from the initial velocity field should be as small as possible. Consequently, the objective function of the optimization process is [19, 29]:

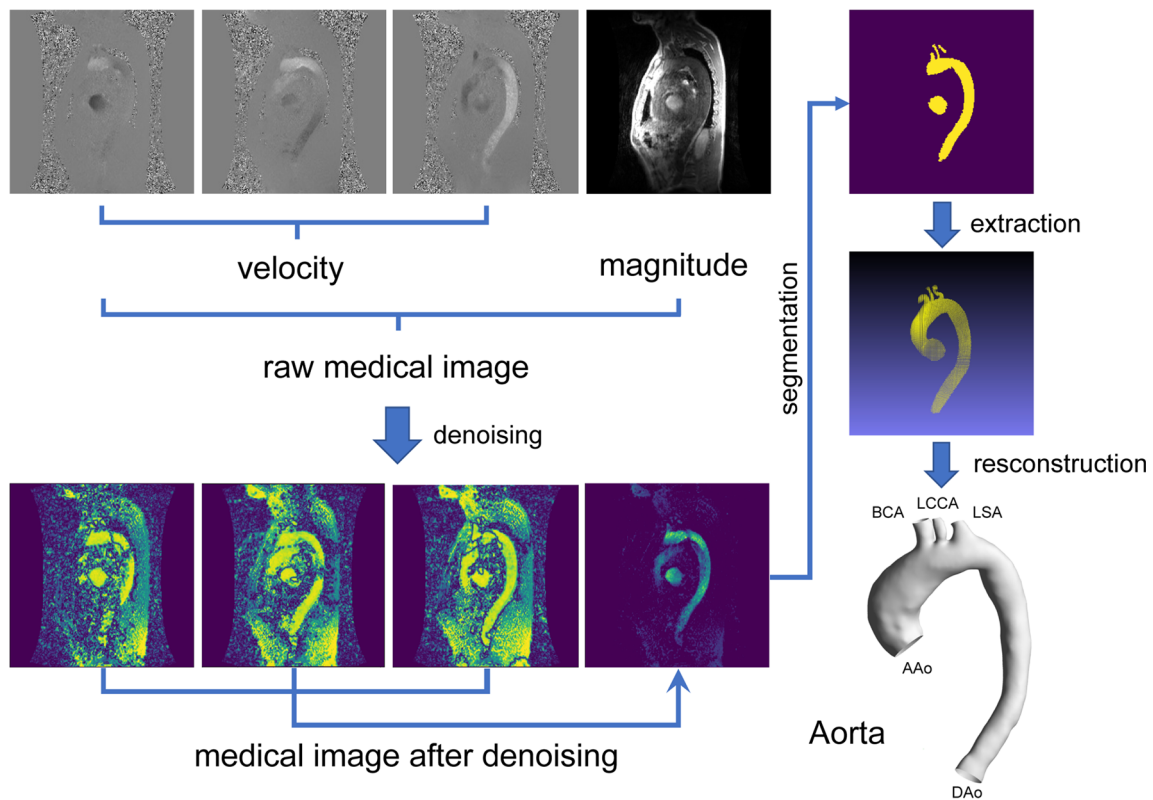


**Fig. 1** The 4D flow MRI data processing stages from the raw medical image to the morphological model of the aorta. The aortic region can be seen clearly after denoising. Then, the aortic area can be detached by segmentation and the point cloud of the aorta can be extracted subsequently. Based on the Poisson surface reconstruction,

morphological model of the aorta is obtained. MRI: magnetic resonance imaging; AAo: ascending aorta; BCA: brachiocephalic artery; LCCA: left common carotid artery; LSA: left subclavian artery; DAo: descending aorta

$$J(\mathbf{U}) = (\mathbf{U} - \mathbf{U}_m)^T(\mathbf{U} - \mathbf{U}_m) + sR(\mathbf{U}), \text{ subject to } \nabla \cdot \mathbf{U} = 0 \quad (7)$$

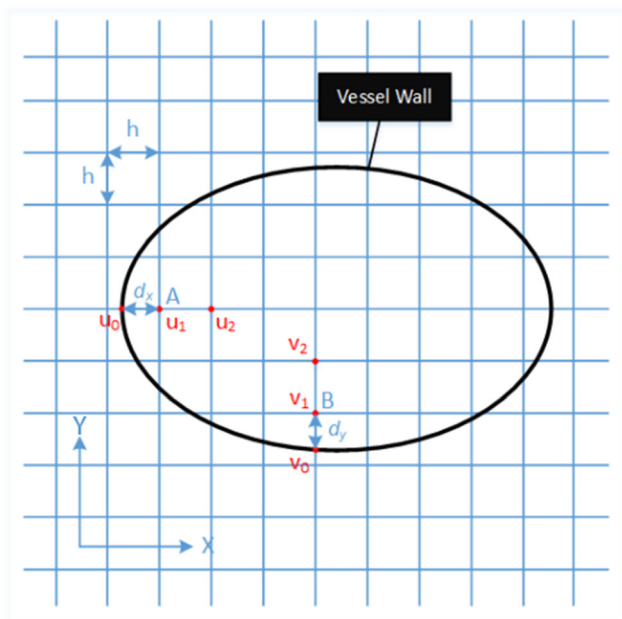


**Fig. 2** 2D schematic of velocity grid and vessel wall (solid black curve)

where  $\mathbf{U}$  is the column vector  $[\mathbf{u}, \mathbf{v}, \mathbf{w}]^T$  consisting of three velocity components and represents the optimization velocity,  $\mathbf{U}_m$  is the column vector  $[\mathbf{u}_m, \mathbf{v}_m, \mathbf{w}_m]^T$  consisting of three velocity components and represents the original measurement velocity,  $(\mathbf{U} - \mathbf{U}_m)^T(\mathbf{U} - \mathbf{U}_m)$  represents residual sum-of-square (RSS) between the optimization velocity and the original measurement velocity,  $R(\mathbf{U})$  reflects the smoothness of the velocity field, and smoothing parameter  $s$  is a positive value. The larger  $s$  is chosen, the smoother velocity field will be. In this work, the second derivative of velocity is used to characterize the smoothness of the flow field, namely:

$$R(\mathbf{U}) = \|\mathbf{D}\mathbf{U}\|^2 = \mathbf{U}^T \mathbf{D}^T \mathbf{D} \mathbf{U} \quad (8)$$

where  $\mathbf{D} = \frac{\partial^2}{\partial x^2} + \frac{\partial^2}{\partial y^2} + \frac{\partial^2}{\partial z^2}$  is discrete second-order derivative operator, and  $\nabla \cdot \mathbf{U}$  is the divergence of velocity, which can be reformatted with discrete divergence operator  $\mathbf{A}\mathbf{U}$ . Note that the operators  $\mathbf{A}$  and  $\mathbf{D}$  in the near-wall region need to be discrete in terms of Eqs. (5) and (6), while the central difference scheme will be used in the inner area.

According to the Lagrange multiplier method, the original objective function  $J(\mathbf{U})$  can be transformed into a new format  $L(\mathbf{U})$ :

$$L(\mathbf{U}, \lambda) = (\mathbf{U} - \mathbf{U}_m)^T (\mathbf{U} - \mathbf{U}_m) + sR(\mathbf{U}) + 2\lambda^T \nabla \cdot \mathbf{U} \quad (9)$$

where  $\lambda$  is the Lagrangian multiplier. The first derivative of  $\mathbf{U}$  and the first derivative of  $\lambda$  are set to be zero. Therefore, the following linear equations can be obtained by minimizing the objective function,

$$\begin{cases} (\mathbf{I} + s\mathbf{D}^T\mathbf{D})\mathbf{U} + \mathbf{A}^T\lambda = \mathbf{U}_m \\ \mathbf{A}\mathbf{U} = 0 \end{cases} \quad (10)$$

where  $\mathbf{I}$  is a unit matrix, and further arrangement to the linear equations show as

$$\begin{bmatrix} \mathbf{I} + s\mathbf{D}^T\mathbf{D} & \mathbf{A}^T \\ \mathbf{A} & 0 \end{bmatrix} \begin{bmatrix} \mathbf{U} \\ \lambda \end{bmatrix} = \begin{bmatrix} \mathbf{U}_m \\ 0 \end{bmatrix} \quad (11)$$

When the smoothing parameter  $s$  is given, the optimized velocity field  $\mathbf{U}$  can be obtained by solving the linear equations using the minimum residual method which is a least squares minimization procedure for residuals. Equation (11) can be solved by the iterative method, in which the coefficient matrix is sparse. The optimized velocity field  $\mathbf{U}$  can be obtained when the residuals are less than  $1e-3$ .

Since the noise level of the flow field in 4D flow MRI cannot be estimated in advance, the smoothing parameter  $s$  in Eq. (11) needs to be automatically determined based on the flow field data. The choice of  $s$  is optimized by minimizing the generalized cross-validation (GCV) function following the method by Garcia (2010) [29]. The GCV function is defined as follows:

$$GCV(s) = \frac{(\mathbf{U} - \mathbf{U}_m)^T (\mathbf{U} - \mathbf{U}_m) / 3n}{\left\{ 1 - Tr[(\mathbf{I} + s\mathbf{D}^T\mathbf{D})^{-1}] / 3n \right\}^2} \quad (12)$$

where  $n$  is the number of unknowns,  $Tr$  represents the trace of the matrix. According to the character of the matrix,  $Tr[(\mathbf{I} + s\mathbf{D}^T\mathbf{D})^{-1}]$  can be simplified to the following form:

$$Tr[(\mathbf{I} + s\mathbf{D}^T\mathbf{D})^{-1}] = \sum_{i=1}^{3n} \frac{1}{1 + s\lambda_i} \quad (13)$$

where  $\lambda_i$  is the eigenvalue of the sparse matrix  $\mathbf{D}^T\mathbf{D}$ . Due to a large amount of data in a single velocity field of 4D flow MRI, the efficiency of direct equation solving will be very low. In the current work, an approximate solution method is adopted. Since the eigenvalues of  $\mathbf{D}^T\mathbf{D}$  obey the exponential decay law approximately, the eigenvalues are fitted by exponential functions for a quick solution. Firstly, the first 200 maximum eigenvalues are solved accurately. Secondly, the eigenvalue distribution is fitted by the exponential function. Finally, each eigenvalue is calculated approximately according to the fitting result. After finding the  $s$  which makes the  $GCV(s)$  smallest, the velocity field that satisfies both the divergence-free constraint and the smoothness can be acquired by bringing  $s$  back to the formula (11).

## 2.4 WSS estimation

The vessel geometry model is discretized into triangular meshes on the surface. The WSS can be evaluated from the velocity field at each mesh grid. Before calculating WSS, we construct a local coordinate system at each mesh grid, as shown in Fig. 3. In the figure,  $X'$  is the direction of flow velocity;  $Y'$  is the normal direction of the wall, and the origin is located at the mesh grid. The procedure for building the local coordinate system is as follows:

- 1) The spline interpolation is applied to the velocity field along the normal direction. In this study, the interpolation spacing between two adjacent points is equal to the velocity field grid spacing. The first interpolation point is located on the wall and its velocity is set to zero.
- 2) The  $Z'$  direction of the local coordinate system is computed, which should be perpendicular to the wall-normal direction and velocity vector.
- 3) The flow direction  $X'$  is obtained by cross-multiplying the  $Y'$  direction and the  $Z'$  direction.
- 4) The interpolated velocity is projected to the flow direction  $X'$  to get the velocity distribution of  $U'$  in the local coordinate system. Note that the velocity on the wall is zero.
- 5) At last, the profile of velocity  $U'$  is fitted using the Musker model [23], as shown in Eq. (14):

$$U' = u_{\tau} \int_0^{Y^+} \frac{\frac{(Y^+)^2}{k} + \frac{1}{s}}{(Y^+)^3 + \frac{(Y^+)^2}{k} + \frac{1}{s}} dY^+, Y^+ = \rho u_{\tau} Y' / \mu \quad (14)$$

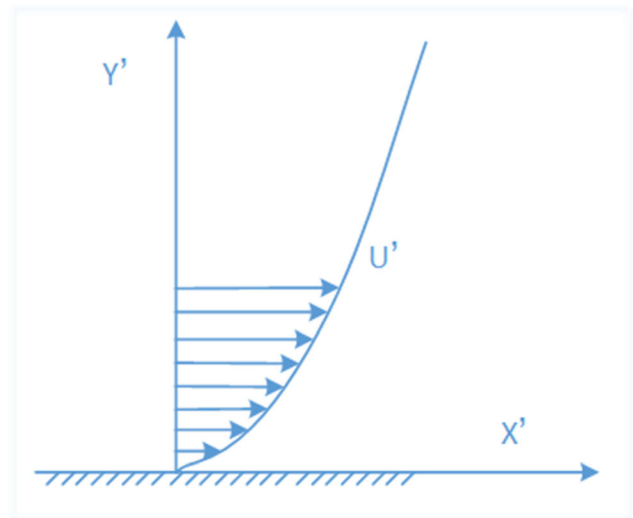


Fig. 3 The local coordinate system

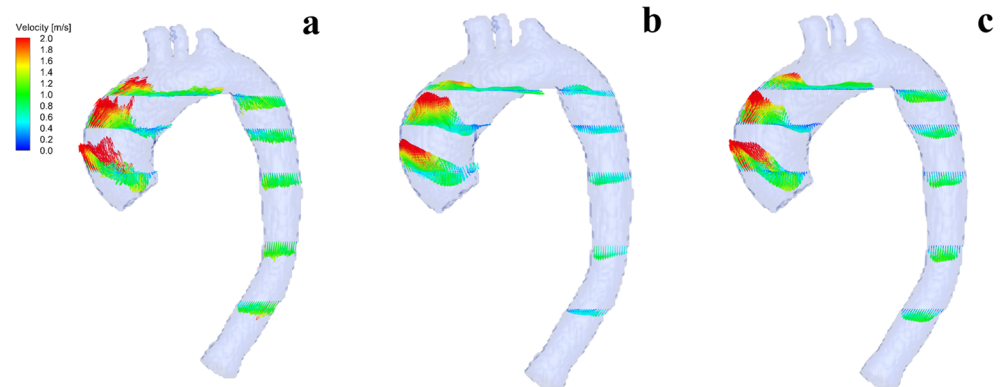
This formula is based on eddy viscosity model, in which the parameters,  $u_\tau$ ,  $\rho$ , and  $\mu$  are the wall friction velocity, the blood density, and the dynamic viscosity coefficient of the blood, respectively. The constants  $k$  and  $s$  are 0.41 and 0.001093, respectively. The only unknown parameter in Eq. (14) is the wall friction velocity  $u_\tau$ , and its optimal value is obtained by curve fitting of local velocity profile. Then,  $u_\tau$  is brought into formula (15) to calculate WSS, and the direction of WSS is consistent with the direction of  $X'$ .

$$\tau = \rho u_\tau^2 \quad (15)$$

## 2.5 CFD method

After the test of mesh-independency (Online Resource 1), 1.6 million cells mesh is chosen for the following calculation. According to the 4D flow MRI flow field data at 30 moments in one cardiac cycle, the velocity distribution optimized by DFS<sub>w<sub>t</sub></sub> method at the entrance of the aorta is extracted at the systolic peak (the fifth timestep of the cardiac cycle). Subsequently, this velocity profile is imposed on the entrance of the computational model and interpolated to the mesh points as the actual inlet velocity boundary condition. An extension with ten times length of the vessel diameter is added at the aorta outlet boundary to minimize numerical problems of convergence and reverse flow, which is typically caused from flow separation and the loss of pressure of distal end. Meanwhile, the resistance model is introduced to simulate the aortic circulation [30, 31]. It is noticed that the aortic wall is inelastic and blood flow cannot pass. The blood is assumed to be Newtonian fluid, in which the density is  $\rho = 1060\text{kg/m}^3$ , and the viscosity is  $\mu = 0.0035\text{Pa} \cdot \text{s}$ . The blood flow is numerically simulated by solving the continuity and the NS equations in ANSYS Fluent (ANSYS Inc. Canonsburg, PA, USA). The “SIMPLE” method is utilized as the coupling of pressure and velocity method, and the second-order implicit method is used to discretize the transient formulation. The k-epsilon RNG model is applied as a turbulent model [32].

**Fig. 4** The comparison of local velocity profile on three circumstances. Original 4D flow MRI (a), 4D flow MRI optimized by DFS method (b), and 4D flow MRI optimized by DFS<sub>w<sub>t</sub></sub> method (c). DFS: divergence-free smoothing; DFS<sub>w<sub>t</sub></sub>: divergence-free smoothing with wall treatment



## 3 Results

### 3.1 Post-processing of 4D flow MRI with DFS<sub>w<sub>t</sub></sub>

In Fig. 4a, original 4D flow MRI velocity field demonstrates the pattern of blood flow in the core region of the aorta. However, the local suspected velocity vector can be seen on the lateral sections. Figure 4b shows the 4D flow MRI velocity field smoothed by DFS method, in which the noise is reduced significantly. Unfortunately, the near-wall velocity is still untreated, and the lack of velocity vector in the core region of descending aorta (DAo) is also notable. As can be seen from Fig. 4c, 4D flow MRI velocity field smoothed by the DFS<sub>w<sub>t</sub></sub> method can not only correctly reserve the initial velocity in the mainstream region, but also improve the velocity field near the wall with better-resolved velocity gradient. Table 1 gives the statistical results of mean value and standard deviation of the divergence under three different circumstances. The DFS<sub>w<sub>t</sub></sub> method manifests the minimum divergence that can be reached among three ways. The difference can also be seen from the distribution of divergence in three vertical sections from Fig. 5 that DFS cannot remarkably reduce the divergence error, especially on the near-wall area.

### 3.2 Comparison of velocity with CFD simulation

Figure 6 shows the streamlines of blood flow, velocity vector distribution, and velocity contour maps in three specific lateral sections at peak systole from optimized 4D flow MRI velocity field and CFD computing result. On the medial side of the ascending aorta (AAo), both 4D flow MRI and CFD show back flow and swirling flow. A high-speed flow region is formed at the greater curvature side of AAo, where blood flow reaches the maximum. There is spiral flow in CFD and subtle flow separation in 4D flow MRI in the anterior segment of the descending aorta (close to Plane 3). At the distal of DAo, velocity magnitude in 4D flow MRI is slightly less than that in CFD. Plane 1 and Plane 3 display a high consistency and similarity in velocity magnitude and distribution of 4D flow MRI and CFD. For plane 2, the velocity distribution in 4D

**Table 1** Divergence of three various flow field

	Original data	DFS	DFS <sub>wf</sub>
<b>Average (1/s)</b>	0.1164	0.0623	0.0074
<b>Standard deviation (1/s)</b>	0.2163	0.1813	0.0087

DFS, divergence-free smoothing; DFS<sub>wf</sub>, divergence-free smoothing with wall treatment

flow MRI is bilaterally symmetric, which is quite different from CFD, and velocity magnitude at LCCA is much smaller in 4D flow MRI than that in CFD.

Table 2 shows the Pearson correlation coefficient and the average differences of velocity in three specific planes extracted from both 4D flow MRI and CFD. The correlation profile between three different velocity components is shown in Fig. 7. Except for Plane 2, the correlations of velocity components are sufficiently high in the other two planes. The Bland-Altman analysis [33] of CFD and DFS<sub>wf</sub> results at 150 random sampling points in the region of AAO is given as well (Online Resource 2).

### 3.3 Comparison of WSS with CFD simulation

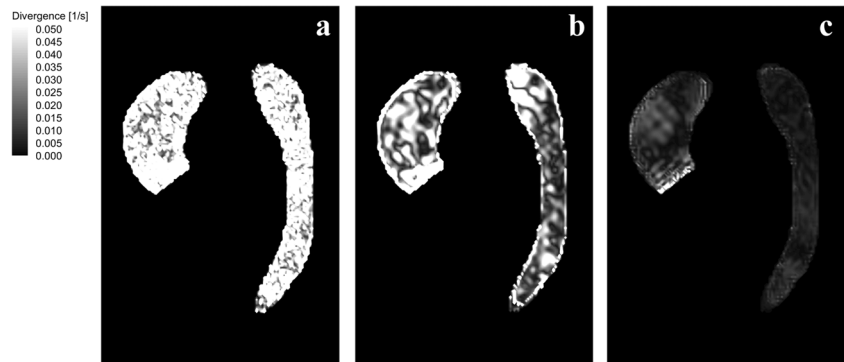
Five wall functions (polynomial model, logarithm model, power model, exponent model, and Musker model) were used to fit the near-wall velocity profile. Musker model showed the best performance in the value and the distribution of WSS (Online Resource 3). WSS obtained from the original 4D flow MRI is discontinuous (see Fig. 8a). Figure 8b shows the WSS computed by smoothed velocity field using DFS method. The distribution of WSS gets smooth, but the magnitude of WSS becomes small, since the smoothness normally reduces the velocity gradient. The maximum WSS decreases from 9.8195 to 4.2326. On the basis of velocity field optimized by DFS<sub>wf</sub> method, WSS has a significant improvement when wall function is applied to ameliorate the velocity profile in the near-wall region, as shown in Fig. 8c. The maximum magnitude of WSS reaches 18 Pa.

The WSS calculated by CFD is shown in Fig. 8d. Generally, for WSS distribution, there is a good consistency between 4D flow MRI improved by wall function and CFD in most regions. WSS calculated from both of them reaches the maximum at the lateral side of AAO, but the magnitude of average WSS coming from CFD is around two times larger of that coming from 4D flow MRI. There are evident differences in supra-aortic vessels (brachiocephalic artery, left common carotid artery, and left subclavian artery) and boundaries where WSS derived from CFD is much higher than that from 4D flow MRI.

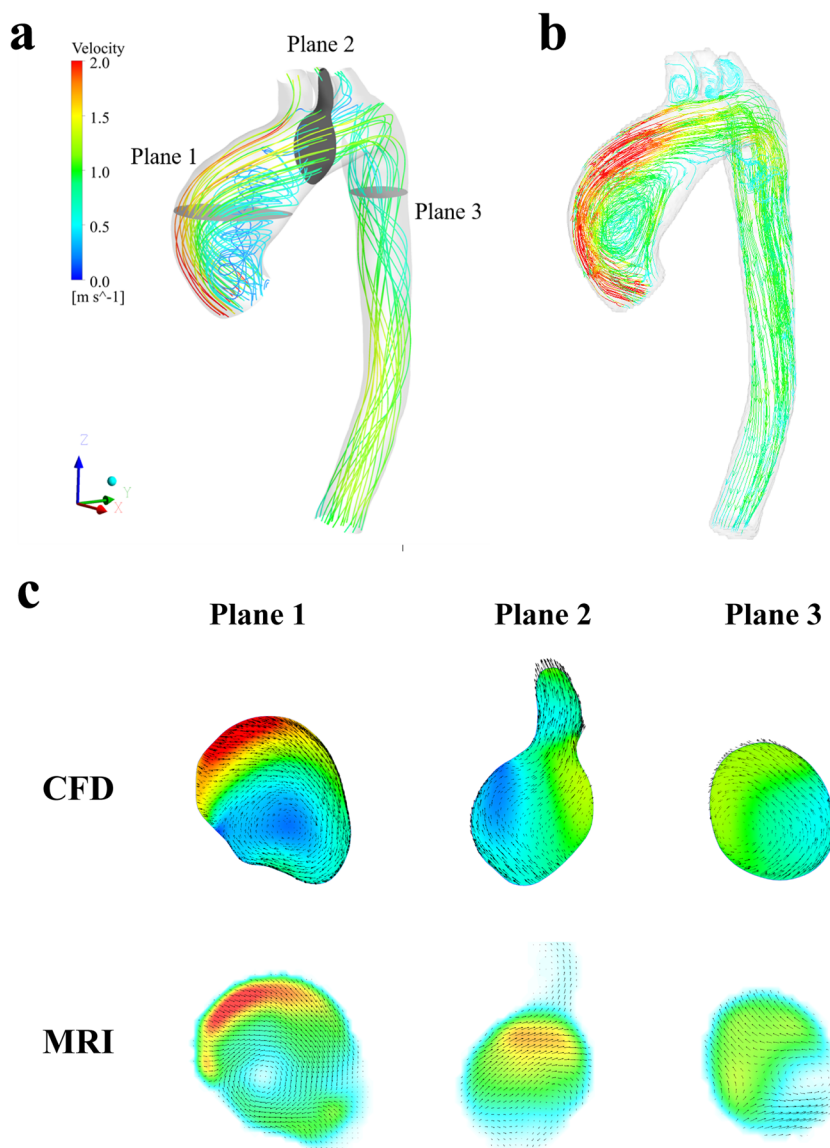
### 3.4 Multi-case visualization of velocity field and WSS

Figure 9a, b gives the comparison of the original 4D flow MRI velocity field and velocity field optimized by DFS<sub>wf</sub> method at peak systole from five cases. From the distribution of velocity vectors, it can be found that the velocity field is remarkably smoothed. The WSS at peak systole calculated from the original 4D flow MRI velocity field with no wall function and the velocity field smoothed by DFS<sub>wf</sub> method with wall function can be seen in Fig. 10a, b. After the application of wall function, the WSS gets more continuous with a significant change on value. Except for the velocity and WSS computed at the systolic peak, a total of 13 moments, 8 in systolic phase and 5 in diastolic phase, in one cardiac cycle are adopted to investigate the performance of optimized 4D flow MRI velocity field and WSS for each case in the dilated region of the aorta (i.e., AAO). In Table 3, the value of divergence gets counted. It is found that the overall average of divergence and the average of standard deviation computed from the smoothed velocity field by DFS<sub>wf</sub> method has obvious reductions. Dynamics of WSS magnitude over the cardiac cycle is depicted in Fig. 11 for the region of AAO. Optimized WSS shows the same trend in value of five cases. The optimized WSS is much higher than that computed from the original 4D flow MRI in the major time of systole. However, during the diastole and the beginning of systole, WSS calculated from the smoothed velocity field by DFS<sub>wf</sub> method with wall function shows the opposite

**Fig. 5** The comparison of divergence distribution on three circumstances. Original 4D flow MRI (a), 4D flow MRI optimized by DFS method (b), and 4D flow MRI optimized by DFS<sub>wf</sub> method (c)



**Fig. 6** Streamlines in the aorta during peak systole. 4D flow MRI processed by DFS<sub>wf</sub> method (**a**), CFD method (**b**), and velocity vectors and contours in three planes for 4D flow MRI and CFD (**c**). CFD: computational fluid dynamics



distribution. At peak systole, case 2 reaches the maximum WSS with a value of 16.5804. The overall average WSS of five subjects at AAo is  $2.7590 \pm 0.9961$  Pa.

**Table 2** Velocity correlation coefficient and average differences in three planes between 4D flow MRI and CFD

	Velocity u	Velocity v	Velocity w
<b>Plane 1</b>	0.8649	0.6469	0.9327
<b>Difference (m/s)</b>	0.0192	0.0756	0.0278
<b>Plane 2</b>	0.5516	0.5690	0.4281
<b>Difference (m/s)</b>	0.1224	0.2461	0.2935
<b>Plane 3</b>	0.7432	0.4317	0.8389
<b>Difference (m/s)</b>	0.0957	0.0040	0.2185

MRI, magnetic resonance imaging; CFD, computational fluid dynamics

### 4 Discussion

For the first testing case, the original 4D flow MRI velocity field contains plenty of noises, dead pixels, and experimental errors. At the same time, the velocity at the wall can be observed, which was mainly caused by the low spatial resolution and partly by the dynamic motion of the aorta. Hence, an optimization for 4D flow MRI velocity field is necessary. 4D flow MRI velocity field smoothed by DFS method shows good smoothness on velocity field and reduction on divergence. Nevertheless, velocity near the wall is still uncorrected because it does not satisfy the wall boundary condition. Meanwhile, the velocity magnitude in the core region of DAo decreases in comparison with the original 4D flow MRI velocity field. To a great extent, the reason is that DFS method does not provide a near-wall treatment. 4D flow MRI velocity field smoothed by the DFS<sub>wf</sub> method has a high

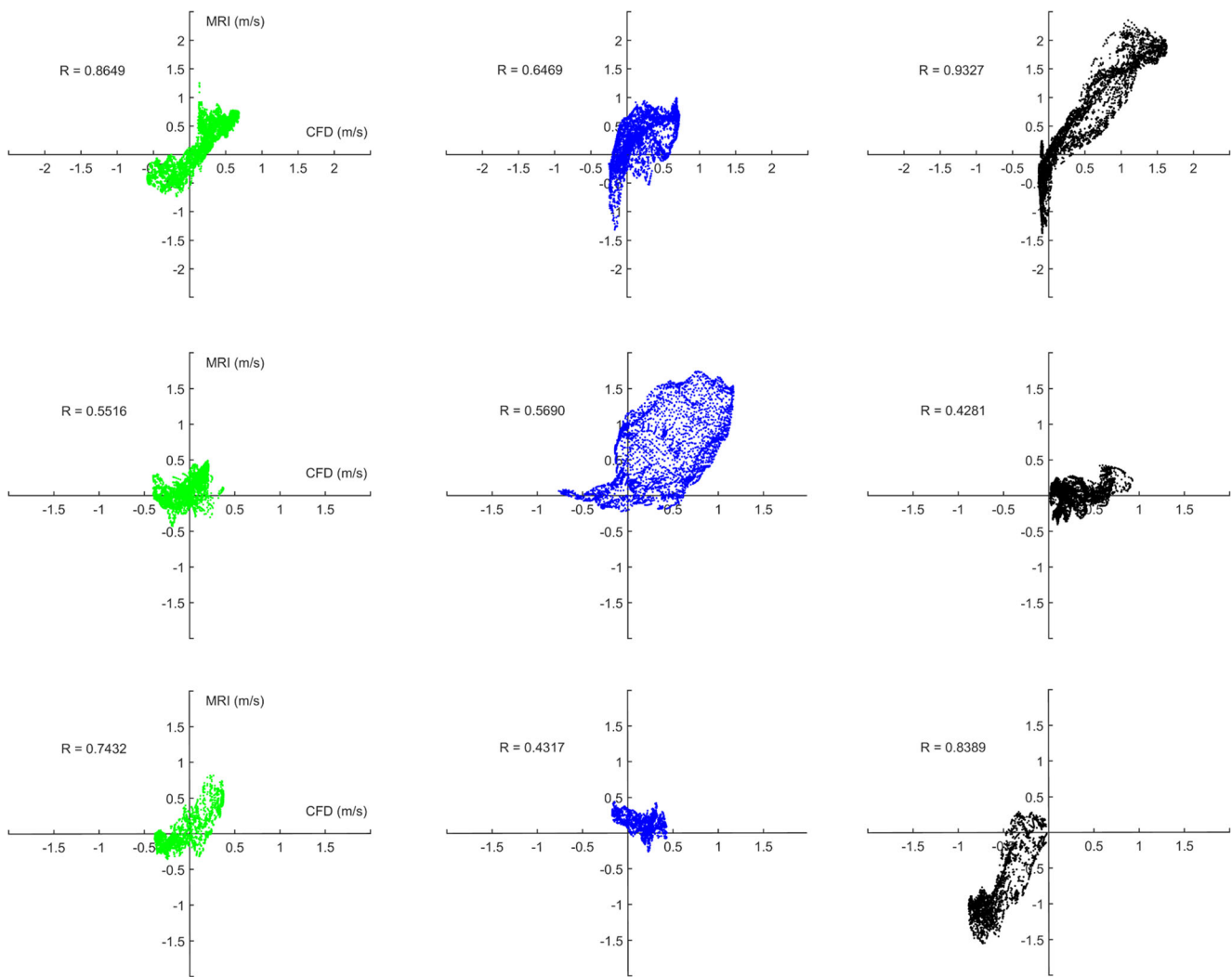


**Fig. 7** The correlation distribution of velocity in three planes between 4D flow MRI and CFD. All *p* values of the results are less than  $1e-6$

coincidence with the original velocity in the mainstream region, and it also satisfies the no-slip wall condition. The gradually reduced divergence value further illustrates the superiority of DFS<sub>wt</sub> method to the 4D flow MRI velocity field. The advantages of DFS<sub>wt</sub> method can also be found from the velocity profiles and divergence values of the other five cases.

In the present study, there is a high-speed flow region with maximum velocity at the lateral side of AAo and helical flow at the inner curvature for both data of 4D flow MRI and CFD during systole. The reason is that the formation of the low-pressure zone and the emergence of flow separation at the AAo near the inner side, which is mainly because the patient suffered from aortic valve stenosis and/or regurgitation. The high-speed flow region extends from the great curvature of the AAo to the aortic arch, and the velocity gradually decreases due to the shunt of the supra-aortic trunks. The great similarity in velocity distribution derived from 4D flow MRI and CFD indicates that 4D flow MRI velocity field optimized by DFS<sub>wt</sub> method presents the intrinsic flow in AAo. Because the

compliance of the aorta in vivo leads to the dilation of the vessel wall during the systolic period, the magnitude and the distribution of velocity have a conspicuous discrepancy in the aortic arch between 4D flow MRI and CFD. Therefore, the flow pattern in the aortic arch region is caused partly by compliance and partly by the tortuous morphological structure in 4D flow MRI [34]. Instead, the flow pattern from CFD in the aortic arch is decided by the geometry when a fixed inlet velocity profile is given [32]. Unsurprisingly, velocity magnitude was quite low, and there was local inverse flow in supra-aortic arteries from 4D flow MRI in the first testing case because of the low resolution [35]. In other words, the velocity field may be underestimated to some extent in 4D flow MRI in supra-aortic vessels compared with CFD results [32]. The flow pattern is comparatively monotonous in DAo, and the velocity is approximately similar in both 4D flow MRI and CFD overall.

WSS calculated from the original MRI velocity field in the first testing case is discontinuous and patchy because of the

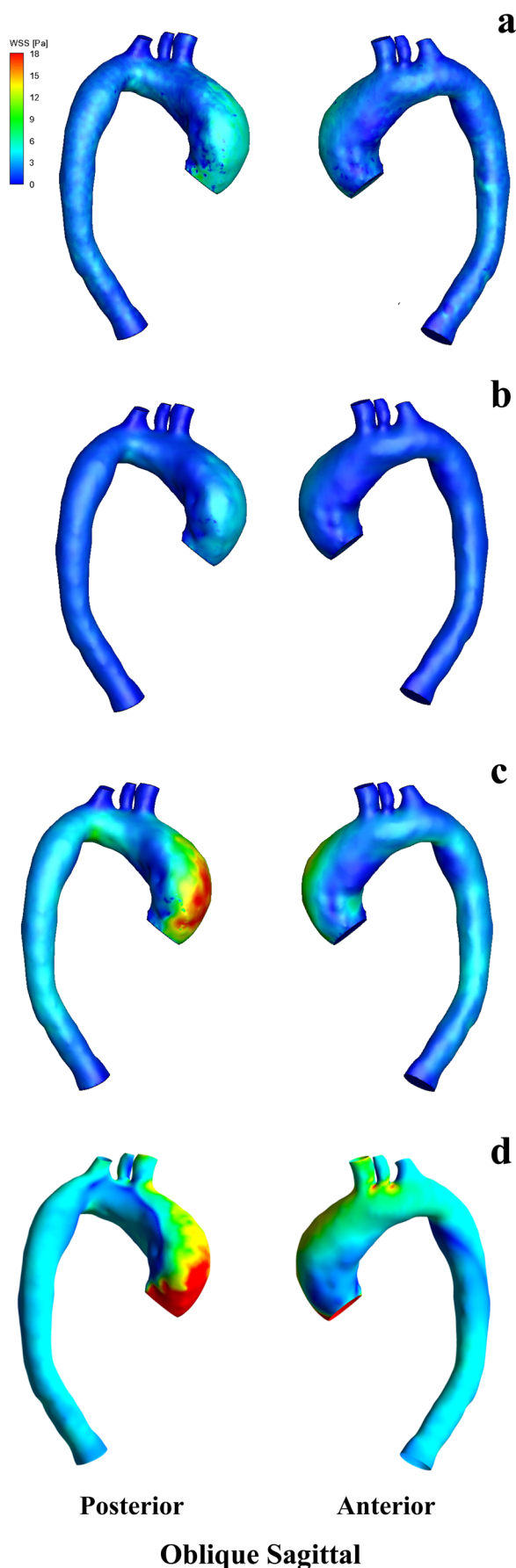


**Fig. 8** WSS comparison in the anterior and posterior side of the aorta in the oblique sagittal images. Original 4D flow MRI without wall function (a), 4D flow MRI optimized by DFS method without wall function (b), 4D flow MRI optimized by DFS<sub>wf</sub> method with wall function (c), and CFD method (d). WSS: wall shear stress

existing of outliers. The velocity is manually set to be zero at the wall boundary during the calculation of WSS. The results of WSS are ameliorated and get smooth when DFS<sub>wf</sub> method is used to optimize the velocity field. This is because noise is substantially reduced, and velocity field satisfies the divergence-free condition at the same time. However, the value of WSS had a slight decrease because of the establishment of new difference equations in the near-wall region to satisfy the no-slip wall condition. It is well known that velocity extracted by 4D flow MRI suffers from the coarse spatial resolution of imaging, and it would cause errors or underestimate the WSS [36, 37]. Therefore, an implicit wall function based on the eddy viscosity model is used to characterize the velocity profile in the near-wall region on the basis of DFS<sub>wf</sub> method optimized velocity field, and then WSS is calculated. It can be found that WSS increases since the near-wall velocity gradient is better resolved. But WSS almost does not have a change at supra-aortic trunks and exit of DAo. For WSS of the other five cases computed from the DFS<sub>wf</sub>-processed velocity field, it shows the similar results that WSS gets continuous and the value of it reaches relatively high compared to the WSS calculated from the original velocity field. The overall changes are because the 4D flow MRI velocity field is smoothed by DFS<sub>wf</sub> method and the resolving of the near-wall velocity gradient has been improved with the introduction of wall function.

At peak systole, the distribution of WSS shows high similarity in the most area. WSS reaches the maximum at the convex side of AAO in both 4D flow MRI and CFD because maximum velocity gradient presents. The maximum WSS in CFD is proximately two times higher than that in 4D flow MRI. In general, WSS computed from the 4D flow MRI data is prone to be underestimated, and many studies have shown similar problems [36, 38, 39]. The reason is very complicated, and that cannot be completely fixed at this moment. In the current work, WSS calculated from DFS<sub>wf</sub> method with Musker wall function does not bear comparison with CFD result entirely, but both the value and the distribution of WSS have a significant improvement compared to the other works [40–43]. This improvement also proved the advantages of the proposed method, whereas the problems are still not completely solved. The WSS is much smaller at supra-aortic arteries and boundary area in 4D flow MRI compared to that in CFD. The reason may be as aforementioned that velocity field is still limited by the insufficient resolution of 4D flow MRI. Thus, the near-wall velocity gradient cannot be completely characterized. In contrast, CFD presented a

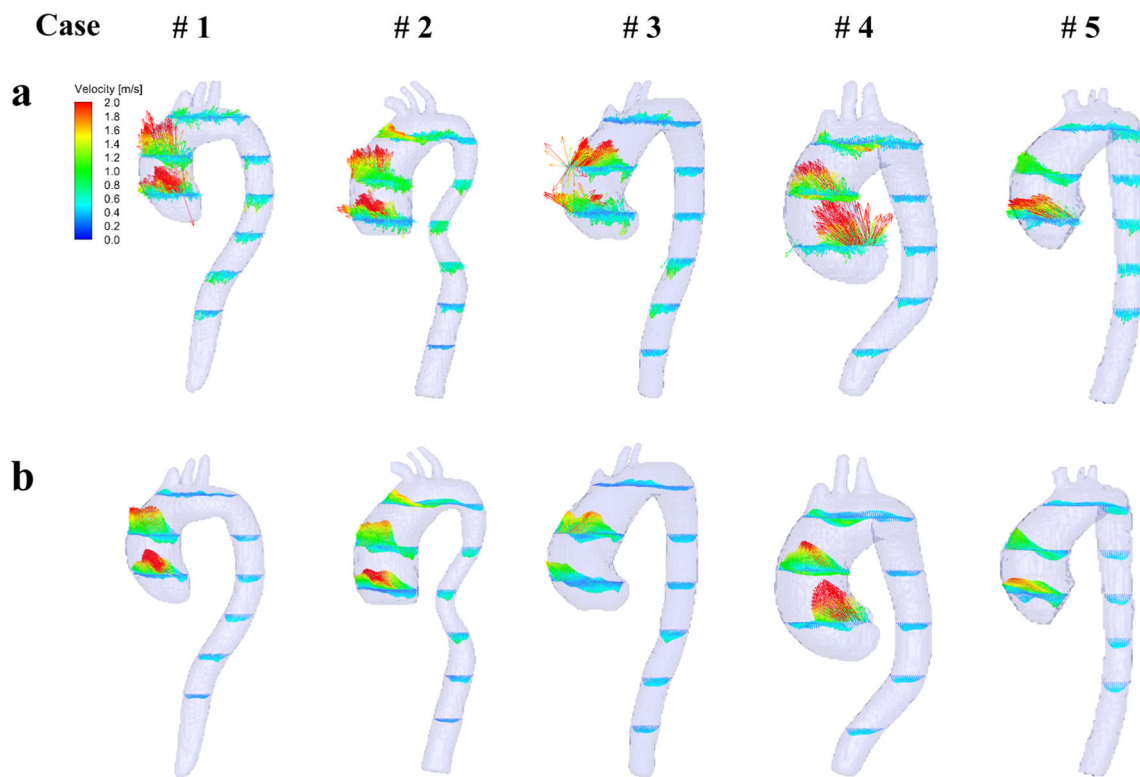


**Fig. 9** The comparison of local velocity profile at peak systole on five cases: original 4D flow MRI (a), 4D flow MRI optimized by DFS<sub>wt</sub> (b)

relatively high WSS. But CFD calculation is highly relying on the proper boundary condition. After all, a wall with biological compliance is known to reduce WSS [30, 44, 45]. Therefore, WSS may be overestimated in CFD in this case. Low WSS area at the proximal of descending aorta can be found in 4D flow MRI because of the flow separation caused by compliance. A similar pattern is also discovered in CFD due to the presence of swirling flow resulted from inflexible and slightly twisted morphology of the aorta.

In one full cardiac cycle, the distribution of WSS magnitude shows high consistency in the region of AAO in five patients. The WSS calculated from the original velocity field with no wall function keeps a relatively high level in both systole and diastole. Even though the original 4D flow MRI velocity field has plenty of noise, the WSS computed from it is still lower in systole. It is because that there is no wall function used to correct the near-wall flow. In diastole and in the beginning of systole, the velocity in the aorta is relatively low, which cannot lead to the high velocity gradient and further induce the high WSS. In fact, the higher WSS is caused by the high noise in velocity field. In systole, because of the introduction of wall function, the WSS calculated from the DFS<sub>wt</sub> optimized velocity field with wall function is larger than that computed from the original velocity field with no wall function. On the contrary, the optimized WSS is lower than that calculated from the original data in diastole. This is because the heart valve

is closed. The flow is gradually reducing from the late systole and almost stagnant during diastole in the aorta. At the beginning of systole, the optimized WSS is normally small but larger than that in the diastole. Because the heart valve is opening, the blood starts to flow out from the left ventricle to the aorta through the heart valve.

The error or uncertainty of medical image processing will definitely affect the DFS<sub>wt</sub> and CFD solutions. For example, due to the insufficient resolution and data noise, the error could be introduced during extracting aortic boundary. This could lead to the inaccurate velocity profile near the boundary. The error might be also accompanied by velocity data optimized by DFS<sub>wt</sub> method. Both problems can further lead to the new error during WSS estimation, which is underestimation of WSS generally. For CFD simulation, it relies on the aortic model and the optimized velocity profile at the entrance of the aorta. Then, the entire velocity field and WSS are simulated based on CFD method. The overestimation of WSS might occur if the simulation wall boundary condition is taken like in this paper. In general, the error of medical image processing is very complicated and different and is not easy to be estimated. How it propagates during the flow simulation or WSS calculation is unknown and hard to be evaluated. The error between DFS<sub>wt</sub> and CFD is mainly caused by different computing methods and by different boundary conditions, such as elastic wall in vivo vs. inelastic boundary condition

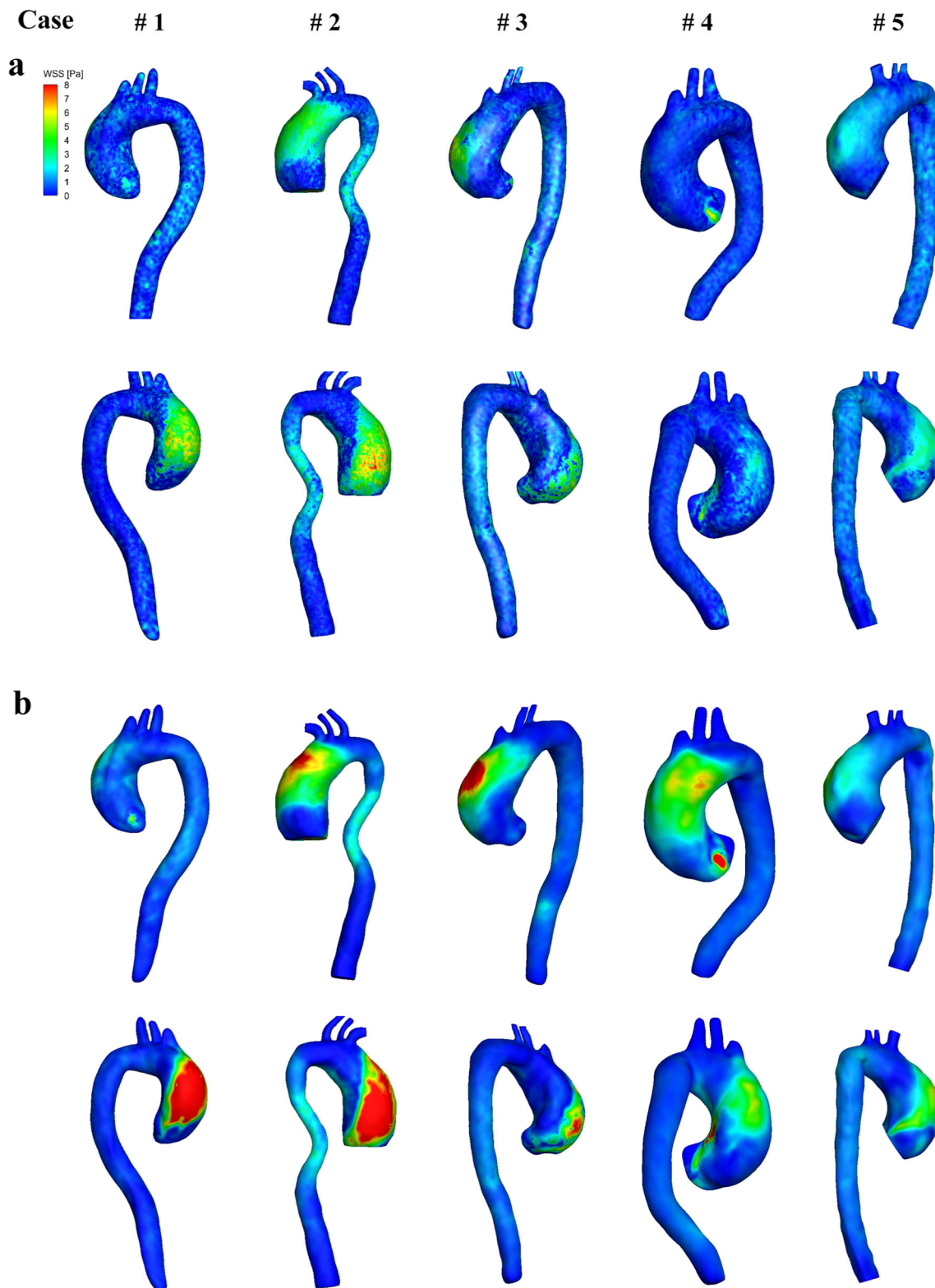


**Fig. 10** WSS comparison in the anterior and posterior side of the aorta at peak systole from five cases: WSS calculated from the original 4D flow MRI with no wall function (**a**), WSS calculated from the 4D flow MRI optimized by  $DFS_{wt}$  with wall function (**b**)

in CFD. Therefore, for the error introduced by image processing or different numerical methods, it will be further

eliminated with the improvement of 4D flow MR technology in future study.

**Table 3** The overall average divergence and average of standard deviation at 13 moments in one cardiac cycle in AAo

Case number	# 1	# 2	# 3	# 4	# 5
<b>Systolic pressure (mmHg)</b>	133	112	121	125	120
<b>Diastolic pressure (mmHg)</b>	78	76	78	75	75
<b>Original 4D flow MRI</b>					
<b>Avg-divergence (1/s)</b>	0.1542	0.1163	0.0928	0.0996	0.0708
<b>Std-divergence (1/s)</b>	0.2094	0.1769	0.1506	0.1599	0.1344
<b>DFS<sub>wf</sub> optimized 4D flow MRI</b>					
<b>Avg-divergence (1/s)</b>	0.0043	0.0040	0.0040	0.0044	0.0038
<b>Std-divergence (1/s)</b>	0.0052	0.0047	0.0042	0.0053	0.0037

*Avg-divergence*, the overall average divergence at 13 moments; *Std-divergence*, the average of standard deviation at 13 moments

There are several limitations to the current work. First, this study is carried out considering six image-based diseased aortas. More healthy or diseased subjects should be enrolled for illustrating the advantages of DFS<sub>wf</sub> method and the reliability of wall function. But for the optimization of velocity field and WSS using DFS<sub>wf</sub> method and wall function in 4D flow MRI, the strategy shows promising results compared with CFD simulation. Second, this paper mainly focuses on the optimization of 4D flow MRI velocity field and the calculation of WSS. More clinical information on patients' aorta should be introduced, and quantitative investigations should be conducted to explore and establish the potential correlation between symptoms and hemodynamic parameters in future work. Third, blood flow is simulated only at peak systole. The velocity distributions could be extracted at the entrance of the aorta from 4D flow MRI at multiple moments in one cardiac cycle. Then, velocity values can be interpolated in time and mapped onto the inlet of computing model. At last, the errors would be introduced to the near-wall velocity if a no-slip wall condition is used based on the assumption of rigid arterial wall. It is beneficial to compute the WSS if elastic arterial wall with moving boundary can be estimated in the future study.

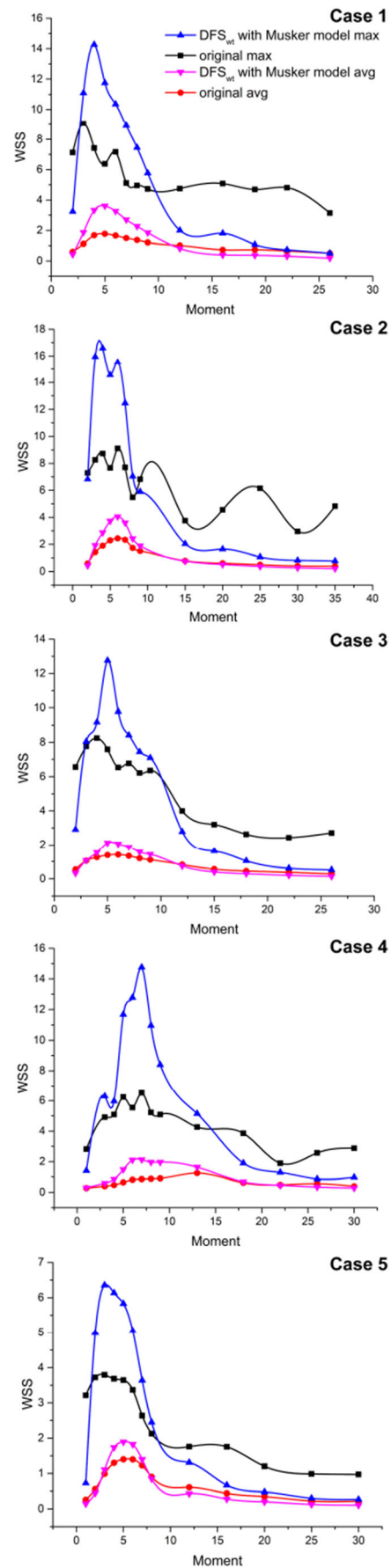


**Fig. 11** Temporal evolution of max and average WSS at 13 moments over one cardiac cycle for both the original data and DFS<sub>wf</sub> method with Musker model optimized data in the region of AAo from five cases. DFS<sub>wf</sub> method with Musker model max: the max WSS computed from the velocity field optimized by DFS<sub>wf</sub> method with Musker wall function; DFS<sub>wf</sub> method with Musker model avg: the average WSS computed from the velocity field optimized by DFS<sub>wf</sub> method with Musker wall function; original max: the max WSS computed from the original velocity field; original avg: the average WSS computed from the original velocity field

## 5 Conclusions

By the comparison of the optimized velocity field in 4D flow MRI and CFD, a strong correlation is found to exist in most regions. The distribution of WSS shows a relatively high similarity with that computed by CFD even with different magnitude of WSS. Inevitably, there are certain differences of velocity and WSS between 4D flow MRI and CFD in aortic boundaries and supra-aortic vessels. Overall, The DFS<sub>wt</sub> method can significantly reduce the divergence of the entire flow field and smooth the flow field, and satisfy the no-slip condition on the wall at the same time. The introduced wall function of velocity profile can better estimate the velocity gradient in the near-wall region and consequently improve the WSS calculation. At peak systole, the overall average WSS of five cases at AAo reaches  $2.7590 \pm 0.9961$  Pa. The total process time of this method is around 3 to 5 min for 4D flow MRI data optimization and hemodynamics evaluation. This means the proposed technique can be performed as part of 4D flow MRI protocol for pathological diagnosis and screening of large cerebral or cardiothoracic vessels, and data analysis can be integrated into a clinically feasible workflow.

**Supplementary Information** The online version contains supplementary material available at <https://doi.org/10.1007/s11517-021-02417-8>.

**Author contribution** Qi Gao, Fei Li, and Xingli Liu made contributions to design this study and draft the manuscript; Shihua Zhao collected MRI data and critically revised the manuscript; Peng Wu, Runjie Wei, Hongping Wang, and Mansu Jin were in charge of post-processing of 4D flow MRI analysis. Wei Wang and Zhaozhuo Niu analyzed clinical data and did substantial contribution to design and critical revision of the manuscript. All authors read and approved the final manuscript.

**Funding** This work was supported by the National Natural Science Foundation of China (grant 12072320).

## Declarations

**Ethics approval** This study was approved by the ethics committee of Fuwai hospital.

**Consent to participate** Written informed consent was obtained from the participant.

**Conflict of interest** The authors declare no competing interests.

## References

- Markl M, Frydrychowicz A, Kozerke S, Hope M, Wieben O (2012) 4D flow MRI. *J Magn Reson Imaging* 36:1015–1036. <https://doi.org/10.1002/jmri.23632>
- Fredriksson AG, Svalbring E, Eriksson J, Dyverfeldt P, Alehagen U, Engvall J, Ebbens T, Carlhäll CJ (2016) 4D flow MRI can detect subtle right ventricular dysfunction in primary left ventricular disease. *J Magn Reson Imaging* 43:558–565
- Szajer J, Ho-Shon K (2018) A comparison of 4D flow MRI-derived wall shear stress with computational fluid dynamics methods for intracranial aneurysms and carotid bifurcations—a review. *Magn Reson Imaging* 48:62–69
- Frydrychowicz A, Berger A, Del Rio AM et al (2012) Interdependencies of aortic arch secondary flow patterns, geometry, and age analysed by 4-dimensional phase contrast magnetic resonance imaging at 3 Tesla. *Eur Radiol* 22:1122–1130
- Lawley CM, Broadhouse KM, Callaghan FM, Winlaw DS, Figtree GA, Grieve SM (2018) 4D flow magnetic resonance imaging: role in pediatric congenital heart disease. *Asian Cardiovasc Thorac Ann* 26:28–37
- Shalhub S, Schäfer M, Hatsukami TS, Sweet MP, Reynolds JJ, Bolster FA, Shin SH, Reece TB, Singh N, Starnes BW, Jazaeri O (2018) Association of variant arch anatomy with type B aortic dissection and hemodynamic mechanisms. *J Vasc Surg* 68:1640–1648
- Tan G, Soon J, Khoo P, et al. (2019) Original Article A review of aortic disease research in Malaysia. 74:67–78
- Hope TA, Markl M, Wigström L et al (2007) Comparison of flow patterns in ascending aortic aneurysms and volunteers using four-dimensional magnetic resonance velocity mapping. *J Magn Reson Imaging An Off J Int Soc Magn Reson Med* 26:1471–1479
- Bogren HG, Buonocore MH, Valente RJ (2004) Four-dimensional magnetic resonance velocity mapping of blood flow patterns in the aorta in patients with atherosclerotic coronary artery disease compared to age-matched normal subjects. *J Magn Reson Imaging An Off J Int Soc Magn Reson Med* 19:417–427
- Biegling ET, Frydrychowicz A, Wentland A, Landgraf BR, Johnson KM, Wieben O, François CJ (2011) In vivo three-dimensional MR wall shear stress estimation in ascending aortic dilatation. *J Magn Reson Imaging* 33:589–597
- Sughimoto K, Takahara Y, Mogi K, Yamazaki K, Tsubota K, Liang F, Liu H (2014) Blood flow dynamic improvement with aneurysm repair detected by a patient-specific model of multiple aortic aneurysms. *Heart Vessel* 29:404–412
- Gallo D, De Santis G, Negri F et al (2012) On the use of in vivo measured flow rates as boundary conditions for image-based hemodynamic models of the human aorta: implications for indicators of abnormal flow. *Ann Biomed Eng* 40:729–741
- Natsume K, Shiiya N, Takehara Y, Sugiyama M, Satoh H, Yamashita K, Washiyama N (2017) Characterizing saccular aortic arch aneurysms from the geometry-flow dynamics relationship. *J Thorac Cardiovasc Surg* 153:1413–1420
- Westerweel J, Scarano F (2005) Universal outlier detection for PIV data. *Exp Fluids* 39:1096–1100
- Gunes H, Rist U (2007) Spatial resolution enhancement/smoothing of stereo-particle-image-velocimetry data using proper-orthogonal-decomposition-based and Kriging interpolation methods. *Phys Fluids* 19:64101

16. Song SM, Napel S, Glover GH, Pelc NJ (1993) Noise reduction in three-dimensional phase-contrast MR velocity measurements. *J Magn Reson Imaging* 3:587–596
17. Busch J, Giese D, Wissmann L, Kozerke S (2013) Reconstruction of divergence-free velocity fields from cine 3D phase-contrast flow measurements. *Magn Reson Med* 69:200–210
18. Ong F, Uecker M, Tariq U, et al. (2013) Improved visualization and quantification of 4D flow MRI data using divergence-freewavelet denoising. In: *Biomedical Imaging (ISBI), 2013 IEEE 10th International Symposium on*. IEEE, 1186–1189
19. Wang C, Gao Q, Wang H, Wei RJ, Li T, Wang JJ (2016) Divergence-free smoothing for volumetric PIV data. *Exp Fluids* 57:15
20. Bousset L, Rayz V, Martin A, Acevedo-Bolton G, Lawton MT, Higashida R, Smith WS, Young WL, Saloner D (2009) Phase-contrast magnetic resonance imaging measurements in intracranial aneurysms in vivo of flow patterns, velocity fields, and wall shear stress: comparison with computational fluid dynamics. *Magn Reson Med An Off J Int Soc Magn Reson Med* 61:409–417
21. Potters WV, van Ooij P, Marquering H, vanBavel E, Nederveen AJ (2015) Volumetric arterial wall shear stress calculation based on cine phase contrast MRI. *J Magn Reson Imaging* 41:505–516
22. Riminarsih D, Karyati CM, Mutiara AB, Wahyudi B (2016) Wall shear stress calculation based on MRI image in patients with abdominal aortic aneurysm (AAA). In: *Informatics and Computing (ICIC), International Conference on*. IEEE, 442–446
23. Kendall A, Koochesfahani M (2008) A method for estimating wall friction in turbulent wall-bounded flows. *Exp Fluids* 44:773–780
24. Li F, Gao Q, Qiao E, Yin G, Zhang RJ, Zhao SH, Wang W (2020) Contributing factor of proximal arch dilation in patients with bicuspid aortic valve—wall shear stress or upward extension of ascending aorta dilation? *Heart Surg Forum* 23:E435–E440. <https://doi.org/10.1532/hcf.2925>
25. Li H, Manjunath BS (1995) Multisensor-Image-Fusion-Using-the-Wavelet-Transform\_1995\_Graphical-Models-and-Image-Processing.pdf. *Graph Model image Process* 57:235–245
26. Huang T, Yang G, Tang G (1979) A fast two-dimensional median filtering algorithm. *IEEE Trans Acoust* 27:13–18
27. Otsu N (1979) A threshold selection method from gray-level histograms. *IEEE Trans Syst Man Cybern* 9:62–66
28. Kazhdan M, Bolitho M, Hoppe H (2006) Poisson surface reconstruction. *Eurographics Symposium on Geometry Processing*
29. Garcia D (2010) Robust smoothing of gridded data in one and higher dimensions with missing values. *Comput Stat Data Anal* 54:1167–1178
30. Lantz J, Renner J, Karlsson M (2011) Wall shear stress in a subject specific human aorta - influence of fluid-structure interaction. *Int J Appl Mech* 3:759–778
31. Uus A (2016) Patient-specific blood flow modelling in diagnosis of coronary artery disease
32. Miyazaki S, Itatani K, Furusawa T, Nishino T, Sugiyama M, Takehara Y, Yasukochi S (2017) Validation of numerical simulation methods in aortic arch using 4D Flow MRI. *Heart Vessel* 32:1032–1044
33. Doğan NÖ (2018) Bland-Altman analysis: a paradigm to understand correlation and agreement. *Turkish J Emerg Med* 18:139–141. <https://doi.org/10.1016/j.tjem.2018.09.001>
34. Kilner PJ, Yang GZ, Mohiaddin RH, Firmin DN, Longmore DB (1993) Helical and retrograde secondary flow patterns in the aortic arch studied by three-directional magnetic resonance velocity mapping. *Circulation* 88:2235–2247
35. Frydrychowicz A, Winterer JT, Zaitsev M et al (2007) Visualization of iliac and proximal femoral artery hemodynamics using time-resolved 3D phase contrast MRI at 3T. *J Magn Reson Imaging An Off J Int Soc Magn Reson Med* 25:1085–1092
36. Stalder AF, Russe MF, Frydrychowicz A, Bock J, Hennig J, Markl M (2008) Quantitative 2D and 3D phase contrast MRI: optimized analysis of blood flow and vessel wall parameters. *Magn Reson Med* 60:1218–1231
37. Oyre S, Ringgaard S, Kozerke S, Paaske WP, Erlandsen M, Boesiger P, Pedersen EM (1998) Accurate noninvasive quantitation of blood flow, cross-sectional lumen vessel area and wall shear stress by three-dimensional paraboloid modeling of magnetic resonance imaging velocity data. *J Am Coll Cardiol* 32:128–134
38. Cibis M, Potters WV, Gijzen FJ, Marquering H, van Ooij P, vanBavel E, Wentzel JJ, Nederveen AJ (2016) The effect of spatial and temporal resolution of cine phase contrast MRI on wall shear stress and oscillatory shear index assessment. *PLoS One* 11:1–15. <https://doi.org/10.1371/journal.pone.0163316>
39. Garcia J, Barker AJ, Markl M (2019) The role of imaging of flow patterns by 4D flow MRI in aortic stenosis. *JACC Cardiovasc Imaging* 12:252–266. <https://doi.org/10.1016/j.jcmg.2018.10.034>
40. Rodríguez-Palomares JF, Dux-Santoy L, Guala A, Kale R, Maldonado G, Teixidó-Turà G, Galian L, Huguet M, Valente F, Gutiérrez L, González-Alujas T, Johnson KM, Wieben O, García-Dorado D, Evangelista A (2018) Aortic flow patterns and wall shear stress maps by 4D-flow cardiovascular magnetic resonance in the assessment of aortic dilatation in bicuspid aortic valve disease. *J Cardiovasc Magn Reson* 20:28. <https://doi.org/10.1186/s12968-018-0451-1>
41. Geiger J, Rahsepar AA, Suwa K, Powell A, Ghasemiesfe A, Barker AJ, Collins JD, Carr JC, Markl M (2018) 4D flow MRI, cardiac function, and T1-mapping: association of valve-mediated changes in aortic hemodynamics with left ventricular remodeling. *J Magn Reson Imaging* 48:121–131. <https://doi.org/10.1002/jmri.25916>
42. van Ooij P, Markl M, Collins JD, Carr JC, Rigsby C, Bonow RO, Malaisrie SC, McCarthy PM, Fedak PWM, Barker AJ (2017) Aortic valve stenosis alters expression of regional aortic wall shear stress: new insights from a 4-dimensional flow magnetic resonance imaging study of 571 subjects. *J Am Heart Assoc* 6:1–14. <https://doi.org/10.1161/JAHA.117.005959>
43. Lenz A, Petersen J, Riedel C, Weinrich JM, Kooijman H, Schoennagel BP, Adam G, von Kodolitsch Y, Reichenspurner H, Girdauskas E, Bannas P (2020) 4D flow cardiovascular magnetic resonance for monitoring of aortic valve repair in bicuspid aortic valve disease. *J Cardiovasc Magn Reson* 22:1–10. <https://doi.org/10.1186/s12968-020-00608-0>
44. Rahiminejad M, Haghighi A, Dastan A et al (2012) Fluid-structure interaction study in rigid and compliant airways. *Acta Mech Sinica* 38:1836–1853

45. Soudah E, Casacuberta J, Gamez-Montero PJ et al (2017) Estimation of wall shear stress using 4D flow cardiovascular MRI and computational fluid dynamics. *J Mech Med Biol* 17:1–14

**Publisher's note** Springer Nature remains neutral with regard to jurisdictional claims in published maps and institutional affiliations.

**Qi Gao** received his bachelor degree from Zhejiang University in 2001, his master degree from Tsinghua University in 2005, and his Ph.D. from the University of Minnesota in 2011. He joined the Beijing University of Aeronautics and Astronautics as an assistant professor in 2011, and was promoted to associate professor in 2013. He moved to Zhejiang University in 2018. Currently, he is an associate professor at the School of Aeronautics and Astronautics, Zhejiang University, China and serves as the Director of Laboratory of Fluid Mechanics at the Institute of Fluid Engineering. Dr. Gao's research is broadly in the area of experimental fluid mechanics. Current projects are focused on developing techniques of volumetric velocimetry and their applications. Studies on turbulent boundary layers and cardiovascular flows are highly interested. Dr. Gao received the Chinese National Award of Technology Invention (second class) in 2018.

**Xingli Liu** obtained his master degree from China Jiliang University in 2017. Currently, he works at Hangzhou Shengshi Tech. Co., Ltd. and serves as the Manager of Department of Fluid Mechanics. He focuses on the simulation study of hemodynamics in cardiovascular diseases and the artificial heart.

**Hongping Wang** received doctor degree in fluid mechanics from Beihang University, China, 2016. Currently, he works as a special research assistant at the Institute of Mechanics, Chinese Academy of Sciences. His research focuses on experimental fluid mechanics and data assimilation.

**Peng Wu** received his master's degree in fluid mechanics from Tsinghua University, China, in 2003, and Ph.D. degree in fluid mechanics from University of Leuven (KU Leuven), Belgium, in 2012. He is currently an associate professor in the Artificial Organs Technology Lab in Soochow University, China. His recent research focus is biofluids. He developed an accurate prediction method for complex internal flows in artificial organs and biological systems. He proposed a novel energy-dissipation-based prediction method for hemolysis and a two-phase flow model for blood stasis. His work also includes cardiovascular fluid mechanics, in particular CFD-based non-invasive diagnosis technique for cardiovascular diseases. He also acted as reviewers for many international journals such as *Biomechanics* and *Modeling in Mechanobiology*, *Artificial Organs*, *International Journal of Artificial Organs*, etc.

**Mansu Jin** acquired her master degree from the Heat/Fluid & Power Engineering at Konkuk university, Korea, in 2016. Her research direction

was experimental study on the nasal airflow inside pre- and post-surgery models. She works as a fluid mechanics engineer at Hangzhou Shengshi Tech. Co., Ltd. She currently focuses on experimental study on the cardiovascular model and heart pump.

**Runjie Wei** received doctor degree in Mechanics from Beihang University, China, in 2002. He is working as the CTO of MicroVec Inc., and in charge of the PIV technic and product explore, and being CTO of Hangzhou Shengshi Tech. Co., Ltd. in 2017. He was good at optic measurement and experimental technics, also published several papers with PIV and *Experimental Fluid Mechanics*, including *EIF JFM*. In 2019, he was awarded the National Technological Invention Award.

**Wei Wang** obtained the bachelor degree in 1984 from Beijing Medical College. In 1998, he got the doctor degree from Peking Union Medical College. From 1984 to 2000, he worked as a cardiac surgeon in Fuwai hospital. From 2001 to 2002, he engaged in postdoctoral research in Tennessee State University. In 2003, he moved to University of California, Los Angeles for postdoctoral research. Since 2004, he back to Fuwai hospital and worked as a cardiac surgeon until now. He is the chief and professor of department of structural heart disease. His research field focuses on the pathogenesis and clinical treatment of aortic valve disease, and the mechanical mechanism in the development of aortic aneurysm.

**Zhaozhuo Niu** obtained the bachelor degree in 1998 from Tongji Medical College of Huazhong University of Science and Technology. In 2004, he got the master degree from the Medical College of Qingdao University. In 2014, he got the doctor degree from the Medical College of Shandong University. From 2015 to 2016, he had accepted the fellowship training of the cardiac surgery in the University of Ottawa Heart Institute. He has worked as a cardiac surgeon since 2001, and skilled in adult cardiac surgery procedures. His research field focuses on the combination between the computational fluid dynamics and the bypass procedure and artificial heart assistance.

**Shihua Zhao** obtained the bachelor degree in 1985 from Anhui Medical University. In 1988, he got the master degree from Peking Union Medical College. Since 1988, he worked as a radiologist in Fuwai hospital. He is the chief and professor of department of magnetic resonance imaging. His research field focuses on the 4-dimensional flow magnetic resonance imaging and the imaging research of cardiomyopathy. Dr. Zhao received the second class prize for scientific and technology progress of China in 2019.

**Fei Li** obtained the doctor degree in 2018 from Peking Union Medical College. He is currently engaged in postdoctoral research in Fuwai hospital & Chinese Academy of Medical Sciences. His research field focuses on the 4-dimensional flow magnetic resonance imaging and the mechanical mechanism in the progression of bicuspid aortopathy.